P24 Comparison of Supercell Maintenance and Dissipation Processes Observed During VORTEX2

Casey E. Letkewicz* and Matthew D. Parker
North Carolina State University, Raleigh, North Carolina

1 INTRODUCTION

The governing dynamics of supercells has been a long-standing area of active research, often with a focus on processes relevant to the developing and mature stages of the storm (e.g., Klemp et al. 1981; Rotunno and Klemp 1982; Davies-Jones 1984; Droegemeier et al. 1993; Weisman and Rotunno 2000; Davies-Jones 2002). Long-lived supercells have been found to be more likely if they are isolated, or are located near preexisting boundaries, which help to locally enhance storm-relative helicity and increase bulk shear (e.g., Atkins et al. 1999; Bunkers et al. 2006a; Bunkers et al. 2006b). Comparatively few studies, however, have examined the processes associated with supercell demise (e.g., Bluestein 2008; Ziegler et al. 2010). Supercell decay has often been attributed to movement into cooler, more stable air (Bluestein 2008), though the mechanisms at work are less certain. It has been hypothesized that as the environment cools, the outflow temperature gradient weakens, thus weakening the storm through stagnation and retrogression of the cold pool (Ziegler et al. 2010) or less baroclinic generation of horizontal vorticity, consequently displacing the cold pool from the storm's updraft (Bluestein 2008). The extent to which these processes actually occur during demise, as well as their generality in all instances of supercell dissipation, is unknown. Observations of supercell dissipation are scarce (Bluestein 2008), but the recent Verification of the Origins of Rotation in Tornadoes Experiment 2 (VORTEX2) field campaign provides a unique dataset of dense observations sampled throughout a storm's lifetime. In order to better understand the governing mechanisms behind supercell demise, this study examines three cases from VORTEX2: two dissipating supercells (9 June 2009 and 15 May 2010) and one elevated supercell (6 May 2010). The analysis methods used to examine the supercells will be presented in Section 2. Next, in Section 3, each case will be evaluated in terms of the changes in its local environment in relation to its evolution, as well as the potential processes that may be at work. Section 4 will then summarize the differences and similarities between the cases, and discuss future work.

*Corresponding author address: Casey E. Letkewicz, Department of Marine, Earth, & Atmospheric Sciences, North Carolina State University, Campus Box 8208, Raleigh, NC 27695–8208. Email: celetkew@ncsu.edu

2 ANALYSIS METHODS

Coordinated sampling of each supercell and its mesoscale environment was achieved with numerous VORTEX2 instrument platforms. In the present study, data from select platforms will be utilized to demonstrate storm-scale morphologies. The inflow environment will be described by soundings launched using the mobile GPS advanced upper air sounding system (MGAUS). During the 2009 field phase, balloons were released in the near-inflow (~30-40 km from the updraft), while in 2010, launches occurred in the near and far (~70-100 km from the updraft) inflow environment. Soundings that did not reach the tropopause were modified using the nearest available sounding in time and space in order to achieve consistent calculations of instability parameters such as convective available potential energy (CAPE) and convective inhibtion (CIN).

Insitu observations of the storm's low-level thermodynamic and kinematic fields were attained via transects throughout the hook-echo and inflow region by the mobile mesonets (Straka et al. 1996), and the StickNets (Weiss and Schroeder 2008). Differences in the nature of the platforms (i.e., mobile vs. stationary), as well as the response times, provides a challenge in terms of direct comparability of the instruments, particularly near strong gradients. However, the use of a time-to-space conversion may mitigate some of the biases associated with mobile vs. stationary instrumentation (Skinner et al. 2010). Each individual instrument also underwent bias-correction based on data collected during a homogeneous period in order to ensure consistent measurements within each platform.

Availability of radar data varied for each case, though sufficient data was collected such that dual-Doppler syntheses could be performed for a substantial portion of their lifetimes. The details of each dual-

Doppler analysis differed according to the radars used (see Table 1), but each case utilized a two-pass Barnes scheme (Barnes 1964) and convergence parameter $\gamma = 0.3$ (Majcen et al. 2008), as well as a correction for storm motion based on nearest WSR-88D's tracking algorithm. The Barnes smoothing parameter κ was consistent between cases and in accordance with the recommendations of Pauley and Wu (1990) and Trapp and Doswell (2000). The three-dimensional wind field was constructed using upward integration of mass continuity with a lower boundary condition of $w = 0$. No extrapolation of the data was performed in order to prevent errors during the synthesis (i.e., errors due to synthesis of winds observed from different heights).

3 VORTEX2 CASES

3.1 9 June 2009

The supercell sampled by VORTEX2 on 9 June 2009 formed in southcentral Kansas just to the cool side of a remnant outflow boundary, quickly maturing and developing strong low-level rotation. However, as the storm propagated deeper into the cool air, the updraft was observed to shrink and completely dissipate. Three near inflow soundings were launched throughout the lifetime of the supercell, at 2319, 2354 and 0056 UTC, with each sounding sampling progressively cool, stable air north of the initiating boundary. Vertical profiles of CAPE, CIN, and delta-z (defined as the vertical distance between the parcel height and its level of free convection; used as a proxy for the amount of lifting required for convection) in Fig. 1 illustrate the modifications to the thermodynamic environment over time. CAPE remained fairly consistent throughout the lifetime of the supercell, maintaining large values sufficient for convection up through approximately 2 km. In contrast, more meaningful modifications were present in the CIN profiles. Inhibition notably increased in the lowest 0.75 km, consistent with the storm moving deeper into the cool, stable air north of the remnant outflow boundary, as well as the effects of diurnal cooling. However, the 1 km layer above 0.75 km contained inhibition that *decreased* over time. This observation, combined with the presence of sufficient instability above 0.75 km, suggests an *elevated* environment favorable for convective maintenance. Furthermore, the amount of lifting required for parcels to reach their levels of free convection (i.e., delta-z in Fig. 1) was virtually unchanged within the storm's lifetime, indicating that no extra work was required for parcels to realize their potential buoyancy as the storm decayed. An interesting question is why the storm was not sustained as an elevated supercell as the low-levels cooled and stability increased. Furthermore, if the presence of increasing CIN was so inhibitive for maintenance, what was the role and contribution of dynamic lifting and how did it evolve? How strong would the dynamic lifting in a supercell need to be to overcome CIN? The failure of the storm to be sustained in an environment with favorable elevated theromodynamics suggests that other processes may have also been at work to result in demise.

An examination of the wind profile in the inflow environment revealed strong modifications within the storm's lifetime. Shear and helicity parameters reflected the evolution of the wind profile, with decreases in 0-6 km bulk shear and effective shear, and strong decreases in 0-3 km and effective storm-relative helicity (Table 2; effective parameters defined as in Thompson et al. 2007). These changes in shear and helicity could impact storm maintenance in a few ways: 1) changes to the rate at which horizontal streamwise vorticity is fluxed into the supercell and tilted into updraft helicity (i.e., nonlinear forcing described in Rotunno and Klemp 1982); 2) changes to the dynamical lifting associated with the "updraft in shear" effect (i.e., linear forcing); 3) cold pool-shear interactions that affect lifting along the supercell's cold pool.

The extent to which the hypothesized effects of the wind profile influenced the storm evolution was explored using dual-Doppler syntheses. The available data suggests that the decreases in shear and helicity (particularly between 2354 and 0056 UTC) coincided with the sharp decreases in vertical velocity and updraft helicity (Figs. 2-3). This storm weakening also coincided with a weakening outflow temperature gradient (Fig. 4), which could impact the strength of low-level lifting (Bluestein 2008; Ziegler et al. 2010) in conjunction with the increasing low-level inhibition. In essence, the demise of this supercell appears to have been the result of an increasingly stable environment, in addition to weaker dynamic lifting.

3.2 6 May 2010

The target storm on 6 May 2010 provides an interesting contrast to the supercell sampled on 9 June 2009 due to the fact that the storm formed above a stable post-frontal airmass, yet persisted for several hours. Two soundings sampled the near and far inflow environment (at 0039 and 0106 UTC launched on 7 May 2010, respectively) reveal the clear elevated nature of the convection with no CAPE in the lowest 1 km (Fig. 5). Additionally, CIN was quite large in the lowest portion of the elevated layer, as was the amount of lifting needed for parcels to reach their LFCs. Despite these inhibitive values, the supercell persisted well into the evening hours, even after coordinated sampling of the storm ceased. In contrast to the 9 June 2009 supercell, the shear and he-

licity parameters in the inflow environment were quite large, each exhibiting *increases* over time (Table 3), suggesting that the dynamical lifting was strong enough to overcome the large inhibition.

Further evidence of the importance of dynamic lifting in this case lies in the mobile mesonet and Sticknet data collected, revealing that the surface appeared to be decoupled from the storm aloft (Fig. 6). The lack of a cold pool at the surface (i.e., no strong temperature gradients due to the absence of penetrative downdrafts reaching the surface, not shown) thus implies that parcel lifting was completely sustained via the dynamic perturbation pressure gradient force, overcoming significant CIN and allowing parcels to achieve buoyancy. In summary, this supercell appears to have been supported by an increasingly favorable inflow environment, with increasing CAPE and an upward trend in bulk shear and storm-relative helicity in the elevated layer.

3.3 15 May 2010

On 15 May 2010, low-level easterly flow impinged upon the mountains in southeastern New Mexico, resulting in orographic lifting and a supercell propagating eastward off of the terrain, eventually dissipating further downstream. Similar to the 9 June 2009 case, profiles of CAPE in the inflow environment underwent relatively little modification over the lifetime of the storm, but CIN showed notable increases, particularly in the ~0.75-1.5 km layer (Fig. 7). Much of these modifications can likely be attributed to inherent environmental inhomogeneities present near orography (i.e., sinking and drying in the lee of terrain producing increased CIN), as well as weaker mesoscale lifting by the topography farther downstream. Vertical profiles of equivalent potential temperature from the inflow soundings (not shown) confirm the presence of stronger mesoscale lifting closer to the terrain and weaker lifting deeper in the lee, which likely had a negative impact on storm maintenance in combination with the increases in deltaz over time (Fig. 7). Idealized simulations of the effects of orography on supercells have also demonstrated that mesoscale flows near terrain influence stability parameters, and consequently the evolution of the storm (Markowski and Dotzek 2011).

In contrast to the previous two cases, the wind profiles on 15 May 2010 appeared to undergo little modification (Table 4). Though clear kinematic trends are admittedly somewhat difficult to parse out due to missing data, there were not any strong decreases in shear or helicity as were present on 9 June 2009. This suggests that weaker dynamic lifting via linear and nonlinear effects did not contribute to storm demise on this day. Furthermore, this is consistent with the simulations of Markowski and Dotzek (2011) that showed that thermodynamic modifications due to orography had a larger influence on storm evolution than terrain-induced changes to the wind profile.

Another factor contributing to storm demise may lie in the evolution of the cold pool. Initial analyses of low-level insitu thermodynamic measurements suggests that the storm outflow became more divergent over time towards the end of its life, surging ahead of the storm, which would consequently weaken low-level lifting necessary to overcome the larger CIN (Fig. 8). Additional analyses are needed, however, to confirm this trend in the outflow and its influence on the supercell's evolution.

4 SUMMARY AND FUTURE WORK

Three supercell cases sampled by VORTEX2 were evaluated in terms of how their changing mesoscale environment impacted their maintenance or demise. One of the similarities between the cases was the presence of sufficient instability for convective maintenance throughout the lifetime of each storm. Each environment also contained varying degrees of convective inhibition; however, one of the main differences leading to varying storm evolutions appears to lie in the presence of sufficient lifting. The 9 June 2009 dissipating supercell inflow environment contained a sharp downward trend in bulk shear and storm-relative helicity, suggesting weaker dynamic lifting that was unable to overcome the increasing low-level CIN. In contrast, bulk shear and helicity was relatively unchanged on 15 May 2010, but the localized support for convection via orographic lifting weakened as the storm moved further into the lee, coincident with larger convective inhibition. Low-level lifting was also weakened in both of these cases as the temperature gradient across the outflow weakened (9 June 2009) or surged ahead of the storm (15 May 2010). The importance of sufficient lifting of parcels for maintenance appears to be given credence when considering the 6 May 2010 environment. Large CIN in the elevated layer was able to be overcome due to large shear and storm-relative helicity, both of which increased over time.

Additional analyses of these cases will be conducted, including the incorportion of more radar data and other insitu measurements in order to achieve complete timelines of storm evolution for each case. Numerical simulations are also currently being run to assess the key physical processes, as well as understand the relative contributions of thermodynamic and kinematic trends in the environment to storm maintenance or demise.

Acknowledgments. The authors would like to acknowledge Conrad Ziegler for beneficial discussions concerning this research as well as the Convective

Storms Group at NC State University for their assistance and feedback. Additional thanks go to the VORTEX2 PIs for making their datasets available. The research reported here is supported by the National Science Foundation under Grant ATM-0758509.

References

Atkins, N. T., M. L. Weisman, and L. J. Wicker, 1999: The influence of preexisting boundaries on supercell evolution. *Mon. Wea. Rev.*, **127**, 2910–2927.

Barnes, S. L., 1964: A technique for maximizing details in numerical weather map analysis. *J. Appl. Meteor.*, **3**, 396–409.

Bluestein, H. B., 2008: On the decay of supercells through a "downscale transition": Visual documentation. *Mon. Wea. Rev.*, **136**, 4013–4028.

Bunkers, M. J., M. R. Hjelmfelt, and P. L. Smith, 2006a: An observational examination of long-lived supercells. Part I: Characteristics, evolution, and demise. *Wea. Forecasting*, **21**, 673–688.

Bunkers, M. J., J. S. Johnson, L. J. Czepyha, J. M. Gryzwacz, B. A. Klimowski, and M. R. Hjelmfelt, 2006b: An observational examination of long-lived supercells. Part II: Environmental conditions and forecasting. *Wea. Forecasting*, **21**, 689–714.

Davies-Jones, R., 1984: Streamwise vorticity: The origin of updraft rotation in supercell storms. *J. Atmos. Sci.*, **41**, 2991–3006.

Davies-Jones, R., 2002: Linear and nonlinear propagation of supercell storms. *J. Atmos. Sci.*, **59**, 3178–3205.

Droegemeier, K. K., S. M. Lazarus, and R. Davies-Jones, 1993: The influence of helicity on numerically simulated convective storms. *Mon. Wea. Rev.*, **121**, 2005–2029.

Kain, J. S., S. J. Weiss, D. R. Bright, M. E. Baldwin, J. J. Levit, G. W. Carbin, C. S. Schwartz, M. L. Weisman, K. K. Droegemeier, D. B. Weber, and K. W. Thomas, 2008: Some practical considerations regarding horizontal resolution in the first generation of operational convection-allowing NWP. *Wea. Forecasting*, **23**, 931–952.

Klemp, J. B., R. B. Wilhelmson, and P. S. Ray, 1981: Observed and numerically simulated structure of a mature supercell thunderstorm. *J. Atmos. Sci.*, **38**, 1558–1580.

Majcen, M., P. Markowski, Y. Richardson, D. Dowell, and J. Wurman, 2008: Multipass objective analyses of doppler radar data. *J. Atmos. Oceanic Technol.*, **25**, 1845–1858.

Markowski, P. M., and N. Dotzek, 2011: A numerical study of the effects of orography on supercells. *Atmos. Res.*, **100**, 457–478.

Pauley, P. M., and X. Wu, 1990: The theoretical, discrete, and actual response of the Barnes objective analysis scheme for one- and two-dimensional fields. *Mon. Wea. Rev.*, **118**, 1145–1163.

Rotunno, R., and J. B. Klemp, 1982: The influence of the shear–induced pressure gradient on thunderstorm motion. *Mon. Wea. Rev.*, **110**, 136–151.

Skinner, P. S., C. C. Weiss, Y. P. Richardson, and P. M. Markowski, 2010: Intercomparison between mobile and stationary surface observing platforms in VORTEX2. Preprints, *25th Conference on Severe Local Storms*, Denver, CO, Amer. Meteor. Soc.

Straka, J. M., E. N. Rasmussen, and S. E. Fredrickson, 1996: A mobile mesonet for finescale meteorological observations. *J. Atmos. Oceanic Technol.*, **13**, 921–936.

Thompson, R. L., C. M. Mead, and R. Edwards, 2007: Effective storm-relative helicity and bulk shear in supercell thunderstorm environments. *Wea. Forecasting*, **22**, 102–115.

Trapp, R. J., and C. A. Doswell, III, 2000: Radar data objective analysis. *J. Atmos. Oceanic Technol.*, **17**, 105–120.

Weisman, M. L., and R. Rotunno, 2000: The use of vertical wind shear versus helicity in interpreting supercell dynamics. *J. Atmos. Sci.*, **57**, 1452–1472.

Weiss, C. C., and J. L. Schroeder, 2008: StickNet–A new portable, rapidly-deployable, surface observing system. Preprints, *88th Annual Meeting of the American Meteorological Society*, New Orleans, LA, Amer. Meteor. Soc.

Ziegler, C. L., E. R. Mansell, J. M. Straka, D. R. MacGorman, and D. W. Burgess, 2010: The impact of spatial variations of low-level stability on the lifecycle of a simulated supercell storm. *Mon. Wea. Rev.*, **138**, 1738–1766.

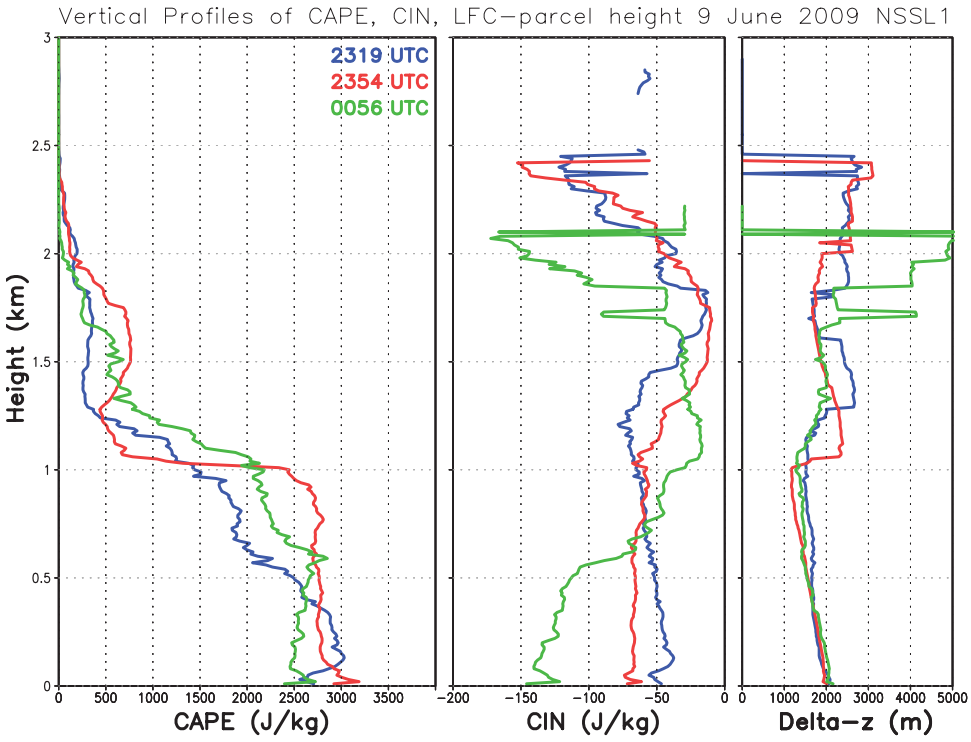

Figure 1: Vertical profiles of CAPE (J kg^{-1}), CIN (J kg^{-1}), and delta-z (vertical distance between parcel height and level of free convection; m) over time from the inflow soundings on 9 June 2009.

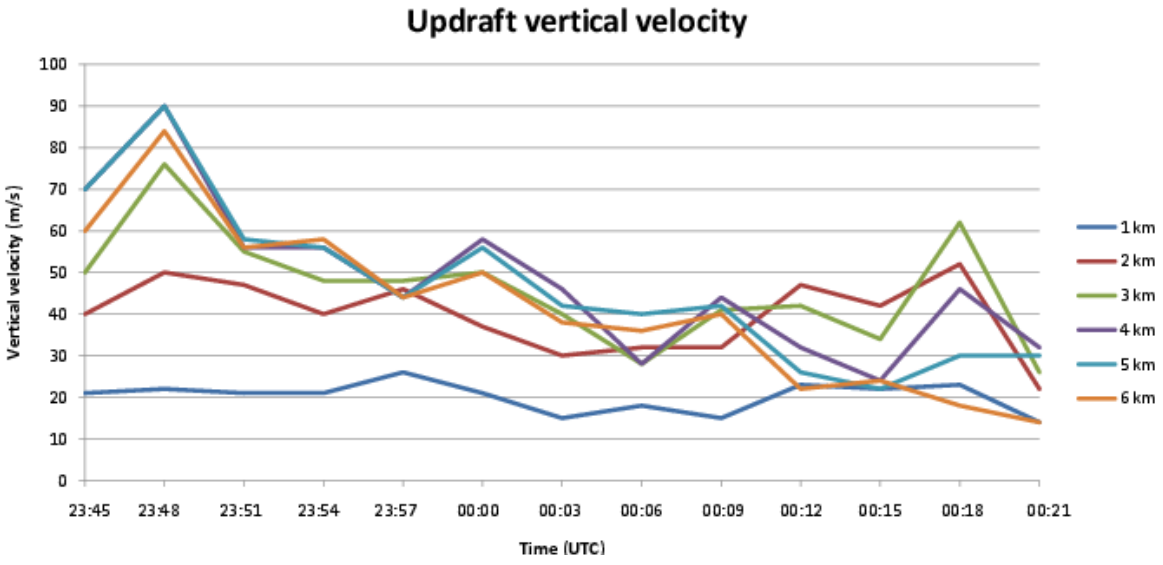

Figure 2: Time series of dual-Doppler derived updraft vertical velocities (m s^{-1}) at several heights on 9 June 2009.

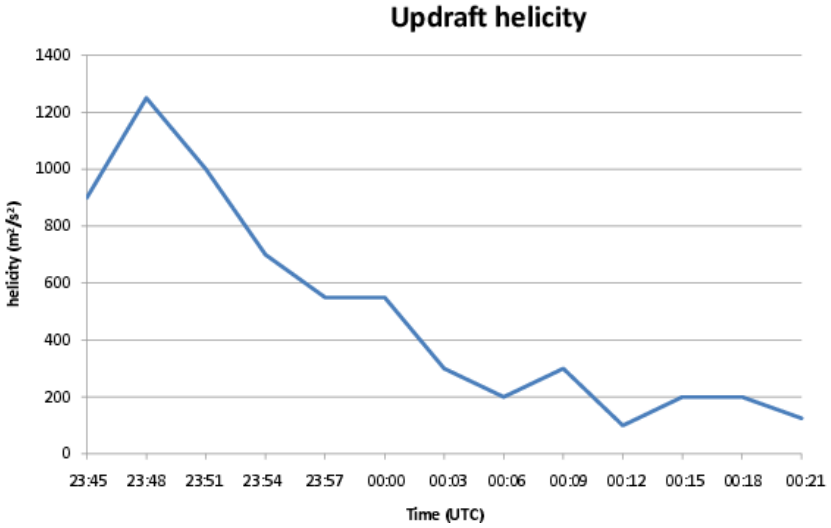

Figure 3: Time series of dual-Doppler derived updraft helicity (m^2s^{-2}) on 9 June 2009, calculated in the manner of Kain et al. (2008).

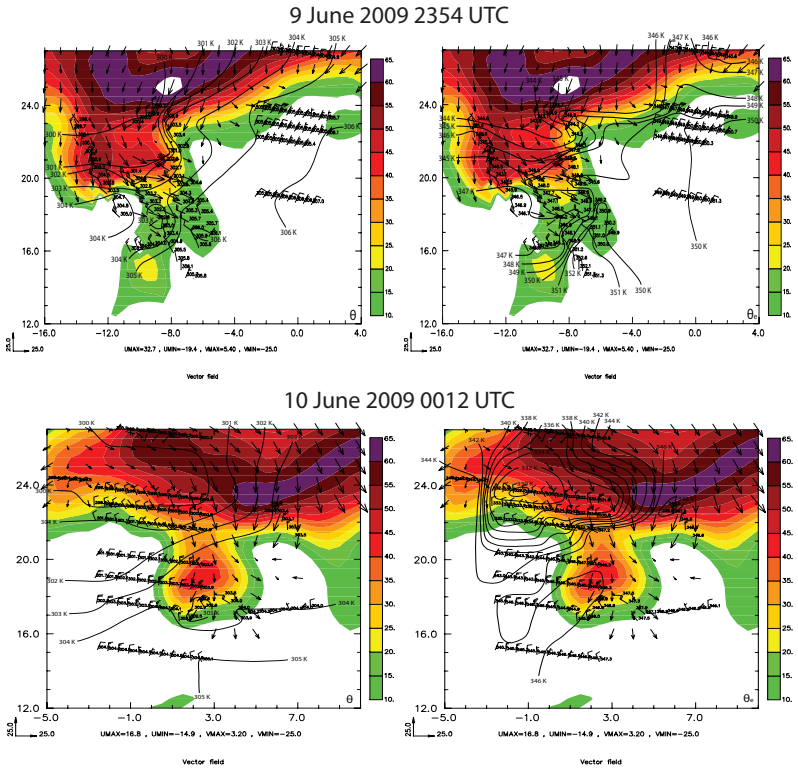

Figure 4: Plan view of radar reflectivity and ground-relative wind vectors (500 m above the surface; derived from SMART-R dual-Doppler syntheses) at 2354 and 0012 UTC 9-10 June 2009, overlaid with time-to-space converted mobile mesonet and Sticknet tracks. Each track is three minutes in length. Thermodynamic fields (θ or θ_e, as labeled) are subjectively analyzed and contoured. The x- and y-axes represent distance in km from the center of the grid (which is the position of SMART-R1).

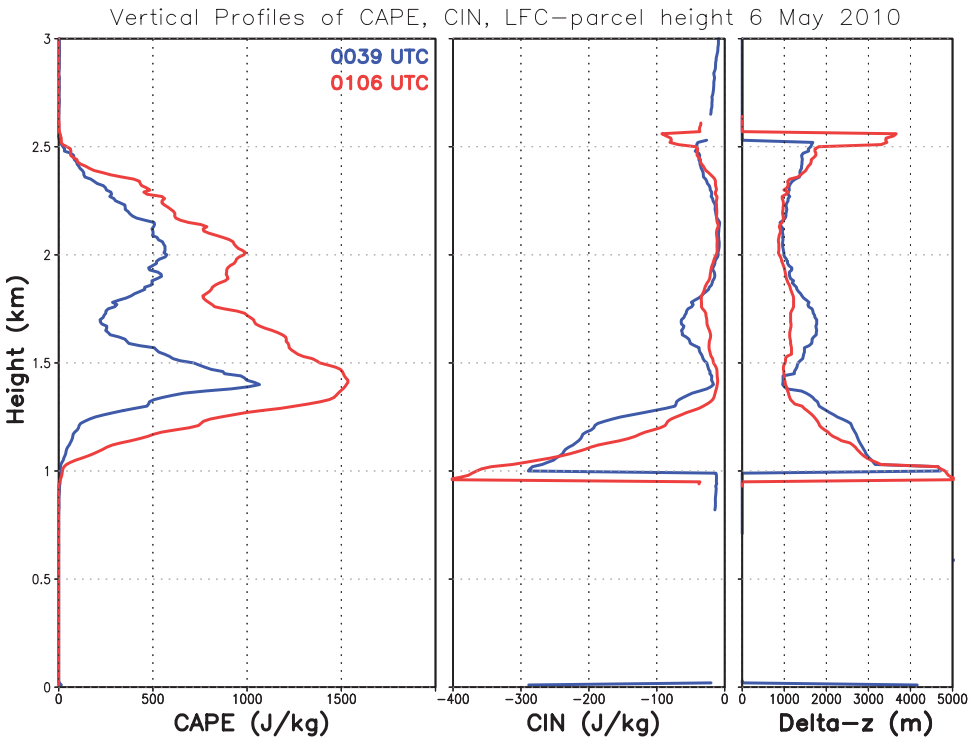

Figure 5: As in Fig. 1, but for the soundings launched for the 6 May 2010 case.

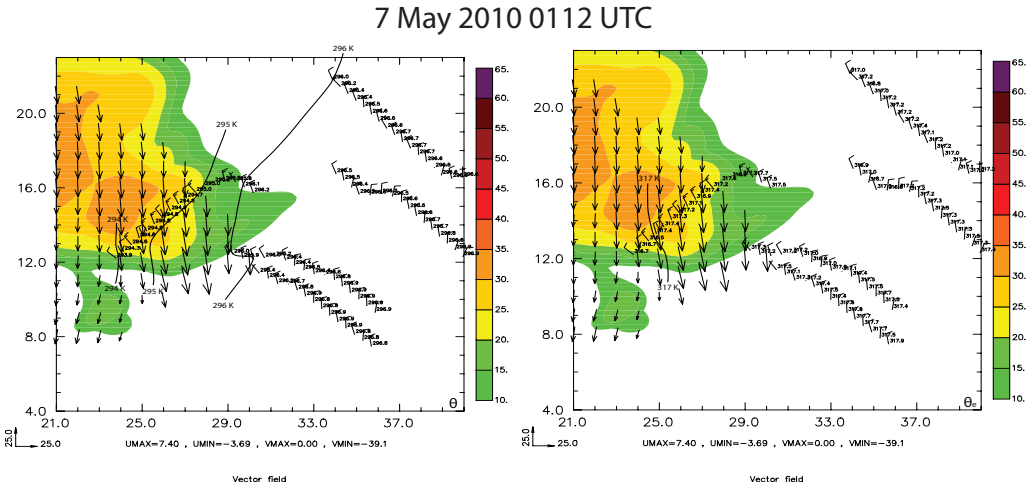

Figure 6: As in Fig. 4, but at 0112 UTC on 7 May 2010. Wind vectors were derived from DOW6/DOW7 dual-Doppler syntheses and the axes represent distance from the position of DOW7.

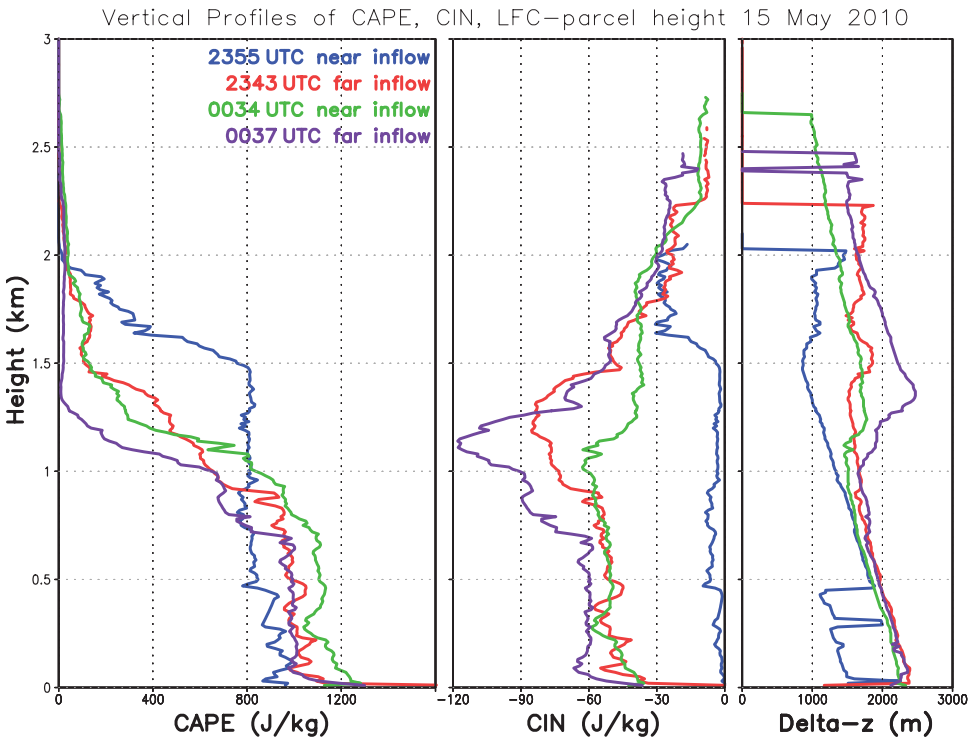

Figure 7: As in Fig. 1, but for the soundings launched for the 15 May 2010 case.

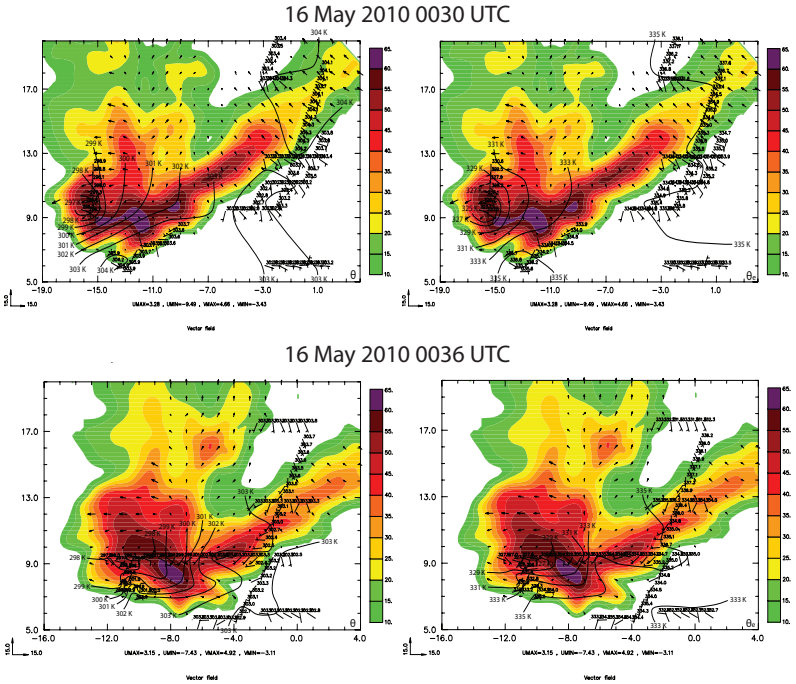

Figure 8: As in Fig. 4, but at 0030 and 0036 UTC on 16 May 2010. Wind vectors were derived from UMass-XPOL/NOXP dual-Doppler syntheses and the axes represent distance from the position of UMass-XPOL.

	9 June 2009	**6 May 2010**	**15 May 2010**
Radars used	SMART-R1, SMART-R2	DOW6, DOW7	UMass-XPOL, NOXP
Grid dimensions ($x \times y \times z$ km)	60×60×15	40×40×5	40×40×5
Horizontal, vertical gridspacing (km)	0.5	0.25	0.25
Barnes smoothing parameter κ (km^2)	1.9	1.09	0.76

Table 1: Dual-Doppler parameters utilized for each case.

	2319 UTC	**2354 UTC**	**0056 UTC**
0-6 km shear (m/s)	32.0	29.0	24.2
0-3 km shear (m/s)	14.8	17.7	20.0
0-1 km shear (m/s)	1.8	5.7	5.9
0-3 km SRH (m^2/s^2)	319	277	124
0-1 km SRH (m^2/s^2)	47	53	-7
effective layer depth (m)	2120	2130	1910
effective shear (m/s)	18.7	19.5	11.2
effective SRH (m^2/s^2)	273	215	68

Table 2: Table of shear and helicity parameters for the observed near inflow soundings on 9 June 2009. "Effective" parameters were defined as in Thompson et al. (2007). Storm-relative parameters were calculated based on storm motions estimated by the Dodge City, KS WSR-88D tracking algorithm.

	Near inflow	*Far inflow*
	0039 UTC	**0106 UTC**
0-6 km shear (m/s)	32.0	35.5
0-3 km shear (m/s)	15.8	14.2
0-1 km shear (m/s)	10.1	12.0
0-3 km SRH (m^2/s^2)	548	747
0-1 km SRH (m^2/s^2)	36	167
effective layer depth (m)	1210	1360
effective shear (m/s)	16.6	20.1
effective SRH (m^2/s^2)	312	385

Table 3: As in Table 2, but for the near and far inflow soundings (as labeled) from the 6 May 2010 case.

	Near inflow	
	2355 UTC	**0034 UTC**
0-6 km shear (m/s)	N/A	28.3
0-3 km shear (m/s)	N/A	19.5
0-1 km shear (m/s)	2.3	3.4
0-3 km SRH (m^2/s^2)	N/A	154
0-1 km SRH (m^2/s^2)	-1	37
effective layer depth (m)	1910	1570
effective shear (m/s)	N/A	10.3
effective SRH (m^2/s^2)	N/A	74

	Far inflow	
	2343 UTC	**0037 UTC**
0-6 km shear (m/s)	N/A	22.8
0-3 km shear (m/s)	13.6	9.7
0-1 km shear (m/s)	2.5	1.3
0-3 km SRH (m^2/s^2)	154	123
0-1 km SRH (m^2/s^2)	37	35
effective layer depth (m)	1520	1220
effective shear (m/s)	7.9	5.7
effective SRH (m^2/s^2)	84	60

Table 4: As in Table 2, but for the near and far inflow soundings (as labeled) from the 15 May 2010 case. Note that some parameters were unavailable ("N/A") due to lost GPS signal at a low altitude.